Eur. Phys. J. B **37**, 229–239 (2004)
DOI: 10.1140/epjb/e2004-00051-y

THE EUROPEAN PHYSICAL JOURNAL B

Transmission of sound through a single vortex

G. Brillant, F. Chillà, and J.-F. Pinton[a]

Laboratoire de Physique CNRS UMR 5672, École Normale Supérieure, 46 Allée d'Italie, 69007 Lyon, France

Received 23 May 2003 / Received in final form 17 November 2003
Published online 15 March 2004 –

Abstract. We investigate experimentally the deformation of acoustic wavefronts after crossing of a single, isolated vortex in free space. The incident sound wavelength can be varied in a large domain. We study the wavefronts at variable distance after transmission through the vortex, when the wavelength and the vortex strength are varied. For small wavelength ($\lambda \ll a$, the vortex core size) our results are in very good agreement with predictions and simulations based on geometrical acoustics principles. However, as the sound wavelength increases to value comparable with the vortex diameter, the deformation of the wavefronts show the development of scattering contributions, with characteristics in agreement with recent theoretical and numerical studies.

PACS. 43.28.+h Aeroacoustics and atmospheric sound – 47.32.-y Rotational flow and vorticity

1 Introduction

We consider the propagation of acoustic waves of weak amplitude in low Mach number flows. In this case, the flow is unmodified by the presence of sound waves, but it changes the sound propagation. It is a situation of theoretical interest for the understanding of wave and matter interactions, and of practical importance because waves can be used as probes for the study of media that interact with them.

Sound waves are longitudinal vibrations; their propagation in a fluid flow is affected by the presence of velocity gradients [1]. For example, let us consider a plane acoustic wave propagating in direction $\boldsymbol{k}$. A non-uniform velocity field advects the wave and thus bends the direction of propagation [3]. In addition, when the characteristic length scale of the velocity gradients is of the order of the sound wavelength, acoustic waves are scattered. A general theory of sound scattering by velocity gradients has been initiated by Lighthill [5]. Numerous subsequent developments have led to the realization that the leading contribution to propagation and scattering effects comes from the antisymmetric part of the velocity gradients, i.e. from the vorticity of the flow [6]. Vortices tend to rotate the wavefronts. In addition unsteady vortices act as sources of sound and this provides a general scattering mechanism: when a sound wave impacts a vortex it advects it harmonically and additional sound is generated at the frequency of the incoming wave.

There is thus a strong motivation to study the interaction of a sound wave with a single isolated vortex (core size a). In the case of small wavelength ($ka \gg 1$ where $k = 2\pi/\lambda$ is the acoustic wave number), theoretical work has been done using geometrical acoustics approximations [2–4] and the associated numerical studies use ray-tracing techniques [7,8]. When the sound wavelength is much larger than the vortex core ($ka \ll 1$), analytical results have been obtained in the Rayleigh scattering regime (cf. [9] and references therein). In the intermediate regime ($ka \sim 1$), the scattering theory of Lighthill [5] has been investigated mainly using the Born approximation, in the limit of far field calculations. Numerical results in the case of a single vortex have been obtained in this regime [9–11].

Experimentally, the scattering of acoustic waves has been used to develop non-intrusive measurement techniques for the study of complex [12,13] and turbulent flows [14–17]. Several measurements of sound transmission in the case of a plane sound wave impacting a single vortex have already been obtained [8,18,19,21,22]. The situation is analogous for the propagation of surface waves across a vortex in shallow water [23–25]. The aim of this paper is to complement these studies. We measure the evolution of the wavefronts as a function of the distance downstream of the vortex. We also take advantage that our experimental setup in air allows us to vary continuously the frequency of the incident sound over a rather wide range: ka covers over a decade, ranging from 4 to 44.

The paper is organized as follows. In Section 2, we give a brief presentation of the apparatus and measurement technique (similar to that used in [21]). Section 3

[a] e-mail: pinton@ens-lyon.fr

is devoted to measurements made in the regime $ka \gg 1$. We study the influence of vortex geometry and strength, we analyze measurements made at varying wavelengths and also at several distances downstream of the vortex. In each case, we note the good agreement between the experimental observations and the results of ray-tracing simulations. In Section 4, we report measurements made when the wavelength of the incident sound is increased so that ka becomes of order unity, and scattering effects become clearly visible.

2 Experimental setup

2.1 Apparatus

The experimental flow belongs to the von Kármán geometry [26]: a strong large scale vortex is produced in the gap between two coaxial corotating discs. Air is the working fluid. The discs, with diameter $2R = 20$ cm, set $H = 27$ cm apart, are driven by DC motors at equal rotation rate $\Omega \in [10, 50]$ Hz kept constant with a PID (Proportional, Integral, Differential) feedback loop. This apparatus is placed at the center of an experimental room whose walls, 3 m away, are covered with sound absorbing material. The flow is insensitive to these lateral boundaries. When the discs are corotating, a strong axial vortex is formed [27]. In order to increase the vortex intensity and stability, we have fitted the discs with a set of blades and covered them with thin discs having a hole in their center [21] – see Figure 1. In this manner we generate vortices with typical strength $\gamma \simeq 1.5$ m^2 s^{-1}, core size $a \simeq 3$ cm (at $\Omega = 30$ Hz). These values are used from previous measurements using hot-wire anemometry [20,21]; a posteriori, they are also found to be consistent with our acoustic measurements.

The aim of our acoustic measurement is to study the transmission of a plane sound wave across an isolated vortex. We generate an incident sound wave with a transducer whose size is large compared to the sound wavelength and we probe the acoustic field with a small size microphone. In order to do so, a capacitive Sell-type transducer [28] (square, edge size $\Lambda = 16$ cm) is used to insonify the vortex. The sound frequency is adjustable in the range $\nu_o \in [7, 100]$ kHz — cf. Figure 1a. The emitter is set at a distance of 66 cm to the discs rotation axis. The sound detector is a miniature B&K microphone (model 4138), placed at an adjustable distance behind the vortex and whose position is varied along a line parallel to the emitter, in 0.5 cm steps controlled by a step motor — cf. Figure 1b. The measured signal is amplified with a B&K preamplifier model 2669B and processed using an EG&G-PAR lock-in amplifier model 5302, to get the in-phase and 90 degrees out-of-phase components. In order to monitor the position of the vortex a local velocity measurement is performed, using a TSI hot wire probe located 7 cm above the lower disc, 4 cm from the rotation axis. All the signals are digitized with a 23-bit HPVXI data acquisition device.

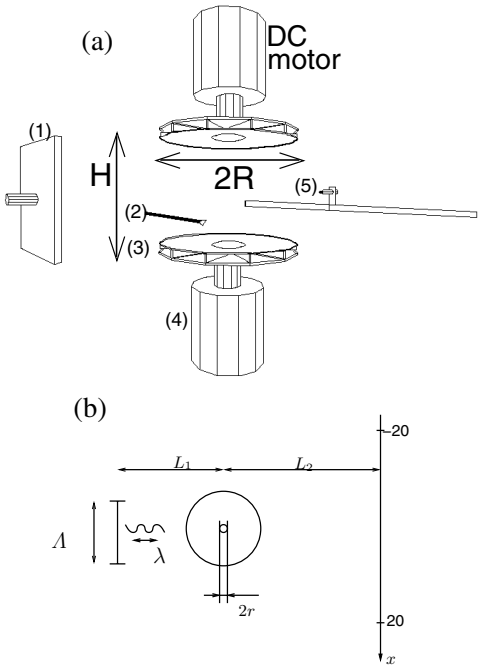

Fig. 1. (a) Sketch of the experimental setup; emitter (1), hotwire probe (2), driving disc (3), motor (4), microphone (5). (b) geometry of the measurement: discs diameter $2R = 20$ cm, set 27 cm apart ($2r = 2$ cm is the diameter of the hole in the thin disc that covers the blades). Distance of Sell emitter to axis $L_1 = 66$ cm, distance axis to microphone L_2 is adjustable. The discs' rotation rate Ω is adjustable in the range $[10 - 50]$ Hz.

2.2 Flow and measurement method

The swirling flow between coaxial corotating discs is made of a large scale vortex upon which turbulent fluctuations are superimposed [27]: the Reynolds number Re of the flow based on the discs' rim speed (or on the vortex circulation) is of the order of 10^5. Velocity measurement made in its neighborhood show a Kolmogorov spectrum, with motion at all scales, from the vortex characteristic size a to the viscous dissipation length $\eta \simeq aRe^{-3/4}$ [29]. Given the typical values of our experiments, this yields a range of scales from $\eta \simeq 300$ μm to $a \simeq 3$ cm – the Taylor microscale of the flow is of the order of 7 mm. In comparison, the range of accessible sound wavelengths in our experiment is $\lambda = c/\nu_0 \in [3.5, 50]$ mm (we use the value $c = 340$ m/s for the speed of sound). The aim of our work is to study the action of the large scale main vortex flow on the incoming sound wave; the effect of the turbulent fluctuations must be averaged out. Note that the flow does not have a spectral gap in space or time scales, that would allow one to define a slowly evolving mean flow plus rapid fluctuations. However, the turbulent fluctuations are incoherent with respect to the large scale flow: averaging realizations of the flow yields the same result as low-pass filtering the velocity field.

Finally, one must take into account the slow precession motion of the vortex [27,30]. In our case the vortex precesses with a period of about 2 seconds, on a circular

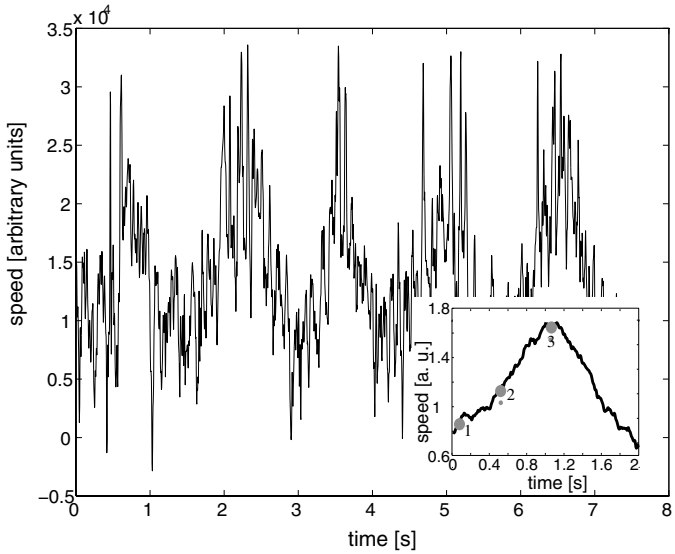

Fig. 2. Velocity 'clock' signal ($\Omega = 30$ Hz). The inset shows the coherent average of one quasi-period of the signal. Black dots mark three particular positions of the vortex in its precession motion, discussed in Section 3.

motion of radius $\simeq 1.5$ cm about the discs axis. This motion is only quasi-periodic: we monitor it using a hot wire probe located nearer to one disc and roughly on the orbit of precession – see Figure 1. The resulting velocity signal is used as a 'clock' to compute an average of the pressure field, synchronous to the position of the vortex [27]. A characteristic signal measured by the hot wire probe is drawn in Figure 2. One clearly notes the quasi-periodic behavior of the vortex precession. Large fluctuations are also observed that are of the order of the signal magnitude. However, these fluctuations are wiped out when a box-car averaging is computed (see Fig. 2 (inset)). Once the average signal is determined, a clock of the precession is obtain and averaging of the sound signal can be done for different vortex position.

Regarding the sound field measurements, we continuously insonify the flow at a fixed frequency with the Sell transducer and we use the microphone to record the pressure field downstream of the vortex (here and in the following, "downstream" refer to "in the incident direction, after propagation through the vortex"). At each location, the pressure field component at the frequency of the sound (phase and amplitude) is coherently averaged over 100 periods of rotation of the vortex, in the manner described above (the phase reference is that of the incident sound). Note that the time of flight of the sound between emitter and microphone is of the order of a few milliseconds: this is fast enough for the large scale flow to be considered "frozen", but not for the small scale fluctuations which have a Kolmogorov time of about 300 μs. We then compare the signal with the reference measurement made in the absence of flow. Acoustic fields (amplitude or phase) are computed as the ratio of the pressure signal detected after transmission through the vortex to the pressure signal recorded in free space when the vortex flow is absent.

3 Measurements at small wavelength

3.1 General features

We first show in Figure 3 the raw profiles, as measured along a line parallel to the emitter plane, both when the fluid is at rest and when the vortex flow is generated by the rotation of the discs. The measurement is made at $\nu_0 = 40$ kHz, corresponding to $ka = 22.1$, a situation that is expected to be within the small wavelength approximation. The amplitude profile in the absence of the flow has the characteristic shape of a diffraction pattern due to the emitter finite size, in the near field region (here $(L_1 + L_2)\lambda/A^2 \simeq 0.3 < 1$). As seen in the figure, this pattern is rotated and altered by the vortex flow. The phase profile, defined as the phase difference with respect to emitter signal, also show the oscillations characteristic of diffraction. When the vortex is present, one clearly identifies the advancing and retardating effects on each side of the vortex axis.

In order to incorporate the diffraction effects, the profiles measured when the fluid is at rest serve as references against which the transmission through the vortex flow is studied: we compute, at the same location in space, the ratio of the amplitude and phase measured when the vortex is generated (triangles in the figure) to the corresponding amplitudes and phases recorded in the absence of flow (circles in the figure).

Using the data shown in Figure 3, one computes the relative phase and amplitude variations shown in Figure 4. Let us first discuss the phase variation. It is advanced when the vortex velocity is in the direction of propagation of the sound wave, and it is retarded on the other side. On dimensional grounds one can show that the phase jump is related to the circulation of velocity about the vortex core, i.e. the vortex strength γ, as [8,21,23]

$$\Delta\Phi = \frac{2\pi\nu_0\gamma}{c^2}. \quad (1)$$

This expression relies on the assumption that the flow about the vortex is axisymmetric, in order to relate the phase jump on each side of the vortex to its circulation (or strength). It can be derived rigorously in the limit of geometrical acoustics [25], as will be indicated in the next section. Schematically, it traces back to the remark that the phase shift corresponds to a displacement Δx of the acoustic wavefront so that $c\Delta x = \gamma$; hence $\Delta\phi = 2\pi\Delta x/\lambda = 2\pi\nu_0\gamma/c^2$. In our setup, one expects phase shifts of the order of a few radians, as observed.

We now turn to the amplitude profile in Figure 4. One observes that the amplitude is smaller than that of the incident sound on the side of the vortex where the phase is advanced, while it is increased on the other side where the phase is retarded compared to the propagation in the fluid at rest. In the context of ray propagation, this can be viewed as defocusing and focusing effects (respectively) downstream of the vortex. Indeed, as can be shown in the small wavelength limit [3,4], the presence of the vortex tends to bend the acoustic rays proportionally to the local

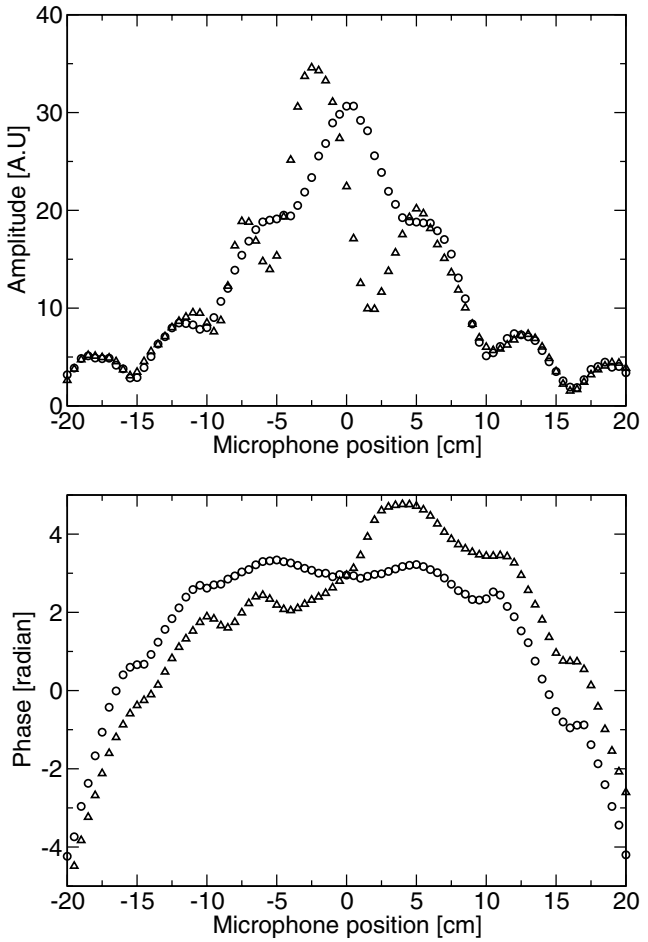

Fig. 3. Raw measurements. (top) amplitude profile downstream of the vortex along a line parallel to the emitter, without flow (○) and with the vortex flow (△); (bottom) corresponding phase profiles, same symbols. (Ω = 30 Hz, ν_0 = 40 kHz, L_2 = 33 cm). The curves are computed as a coherent average as detailed in Section 2.

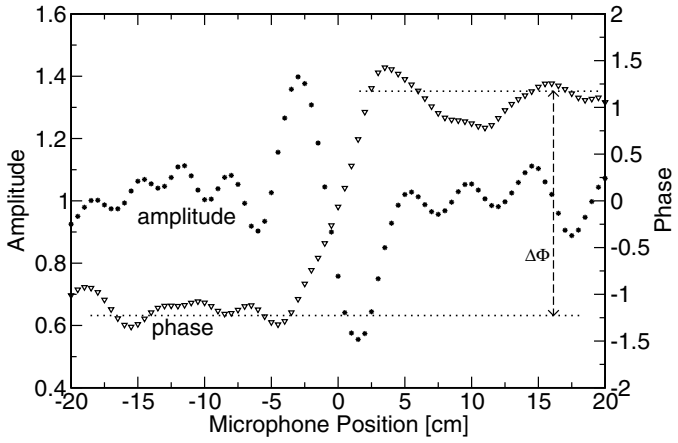

Fig. 4. Typical acoustic measurement, amplitude (circles) and phase (triangles) variations. (Ω = 30 Hz, ν_0 = 40 kHz, L_2 = 33 cm). After the coherent average processing, the points are computed as the ratio of the profiles with and without the vortex flow, as in Figure 3.

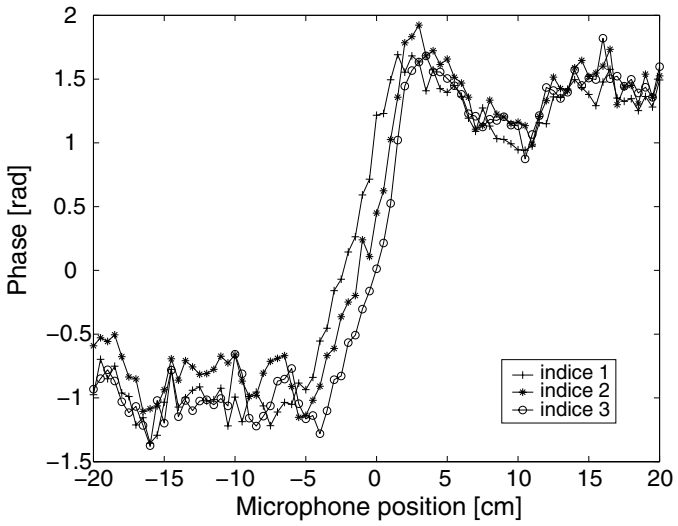

Fig. 5. Phase change of the sound wave downstream of the vortex, at the three positions along its precession motion marked in Figure 2.

vorticity of the flow. With a vorticity distribution being a bell-shaped curve peaking on the vortex axis, one thus finds that the rays are brought together on one side of the vortex (focusing) and set further apart on the other side (defocusing).

We note here that the oscillations on the sides of the phase (and amplitude) profiles have a complex origin that is hard to attribute to a single physical effect; they have the same spatial period as the one due to the emitter diffraction pattern and may be thus due to any small displacement between the measurement with and without the vortex flow (the reflection of sound on the rotating discs may cause such an effect). On the other hand, we cannot rule out scattering effects which could already be present, although $ka > 10$ in the measurement reported here.

We also observe in Figure 5 that the location of zero phase shift, directly aligned with the vortex center line, varies with the position of the vortex along its orbit of precession. Indeed, in Figure 5, the three curves correspond to the three vortex positions marked in Figure 2 (inset).

Compared with other experiments using water as the working fluid [8], the phase jump is quite large. This can be understood if one re-expresses equation (1) as $\Delta\Phi = (a/\lambda)M$, where $M = u_0/c$ is the flow Mach number and a the vortex core size : higher Mach numbers can be achieved in gases than in liquids; in our case the Mach number M is about 0.1. At the Mach numbers reached in air, amplitude variation as large as 50% of the reference amplitude can be observed – see Figure 4. The other advantage of using gases is that sound frequencies are lower – for a given value of ka – so that one can use sampling circuits that offer a high amplitude resolution.

3.2 Comparison with ray-tracing

In the geometrical regime, the sound wave is locally advected by the vortex and the equation of propagation can be written as [2]:

$$\left(\partial_t + \boldsymbol{u}_o \boldsymbol{\nabla}\right)^2 \rho' - c^2 \Delta \rho' = 0, \tag{2}$$

where $\boldsymbol{u}_0$ is the (slow varying) flow velocity and ρ' is the density fluctuations associated with the sound wave. For a sound wave at wavenumber k, one thus obtains for the group velocity:

$$\boldsymbol{V} = c\frac{\boldsymbol{k}}{k} + \boldsymbol{u}_0, \tag{3}$$

from which the variation of the ray direction and phase along its path can be computed. For example, in the small Mach number limit, one obtains with respect to propagation in the fluid at rest, a phase variation of the acoustic wave along a path joining the transmitter (T) and the receiver (R):

$$\delta\Phi_{TR} = \frac{2\pi\nu_0}{c^2} \int_{TR} \mathbf{u}_0(\mathbf{r}) d\mathbf{r} \tag{4}$$

from which one recovers the expression in equation (1) under the assumption of axisymmetry.

Numerically, straight rays are propagated from the Sell emitter in all directions and their phase are unrolled along the rays. Then, the amplitude and the phase of the wave are calculated in each measurement point by summing all the rays that hit this point. Typical experimental and numerical results, drawn in Figure 6, confirm the correspondence of the advance of phase and the defocusing of amplitude. In Figure 6, we also compare our experimental data with a ray-tracing calculation made with a Rankine vortex having the same parameters as measured for the experimental vortex — in the case ($\nu_0 = 40$ kHz, $\Omega = 30$ Hz, $L_2 = 33$ cm) which corresponds to the geometrical acoustics regime (the sound wavelength is a third of the vortex core size). One observes a very good agreement between the computed and measured profiles.

The profiles shown in the figures are computed as the ratio of the acoustic signal in the presence of the vortex to the measurement in free space in its absence. We have checked numerically that the distribution of emission at the Sell transducer (Gaussian or Flat distribution for example) does not modify the amplitude and phase profiles (except for the amplitude of the oscillations on the sides). We also note that the maximum angle θ of deflection of an acoustic ray can be estimated as $\theta_{\max} \simeq \arctan\left(\gamma/4\pi^2 ac\right) \simeq 3 \times 10^{-3}$ rad, which is quite small in our experiment where the maximum downstream distance L_2 is 1.2 m and the acoustic field is measured in 5 mm steps.

3.3 Vortex geometry

As stressed above, the ray trajectory depends on the structure and geometry of the vortex field. In Figure 6, the vortex is assumed to be a Rankine type vortex:

$$V(r) = \begin{cases} \frac{\gamma}{2\pi a}.\frac{r}{a} & \text{if } r \leqslant a \\ \frac{\gamma}{2\pi}.\frac{1}{r} & \text{otherwise} \end{cases} \tag{5}$$

with a core size $a \simeq 3$ cm and a strength $\gamma \simeq 1.4$ m^2 s^{-1}.

In order to test the dependence of the acoustic profiles with different vortex structures, we have also computed other model distributions, such as the Hallock-Burmnham or Lamb types:

$$V_{\text{Hallock-Burmnham}}(r) = \frac{\gamma}{2\pi}\frac{r}{r^2 + a^2}, \tag{6}$$

$$V_{\text{Lamb}}(r) = \frac{\gamma}{2\pi r}\left(1 - e^{-1.2526\left(\frac{r}{a}\right)^2}\right). \tag{7}$$

The acoustic profiles that these vorticity distributions produce (using the same characteristics core size and strength ($\gamma = 1.4$ m^{2}s^{-1}, $a = 3$ cm)) are shown in Figure 7.

One observes little differences on the sides of the acoustic field and only slight differences in the center core region — the central peaks are slightly lower in the case

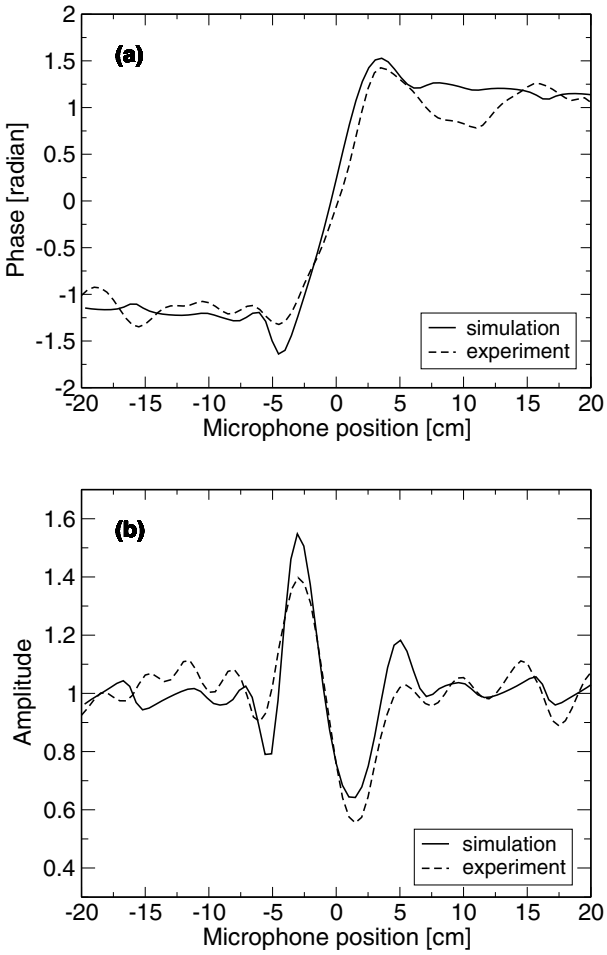

Fig. 6. Ray tracing compared to experimental signal, in the case ($\Omega = 30$ Hz, $\nu_0 = 40$ kHz, $L_2 = 33$ cm). The numerical vortex has a Rankine distribution with the same core size and strength as the experimental one.

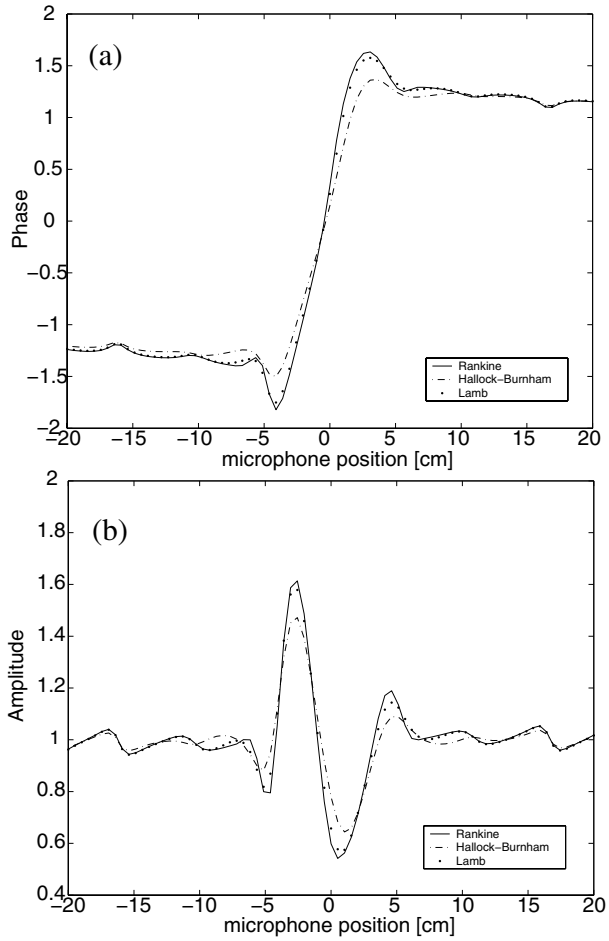

Fig. 7. Acoustic profiles obtained from ray-tracing using several vorticity distributions. In each case the parameters are the experimental ones: $\gamma = 1.4$ m^{2}s^{-1}, $a = 3$ cm, $\nu_0 = 40$ kHz, $L_2 = 33$ cm.

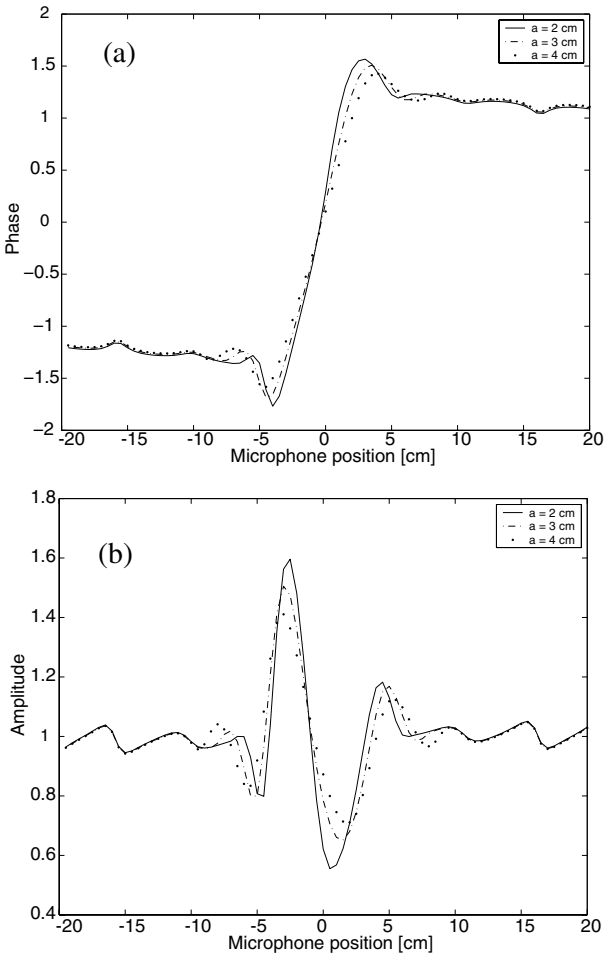

Fig. 8. Impact of the core size on the numerical ray-tracing; ($\gamma = 1.4$ m^{2}s^{-1}, $\nu_0 = 40$ kHz, $L_2 = 33$ cm).

of the Hallock-Burnham vortex than for the Rankine or Lamb vortices. These differences are of the same order as the difference between the experimental measurement and the ray-tracing results. It means that, at least with the statistics available in the measurement reported here, one will not gain an insight as to the precise vorticity distribution which best corresponds to the vortex generated experimentally, but global features such as core size and strength are readily measured. In the same manner, acoustic scattering effects which may be present in the measurement but are not taken into account by the simple ray-tracing modeling used here are difficult to assess in this small wavelength regime. As we will see in Section 4, the scattering effects become much larger as the sound wavelength is increased.

Finally, we have explored numerically the effect of varying the vortex core size. In Figure 8, acoustic profiles have been computed for Rankine vortices of constant strength ($\gamma = 1.4$ m^{2}s^{-1}) and core sizes from $a = 2$ cm to $a = 4$ cm. One observes that the effect is very small on the phase jump. This is again consistent with the fact that the phase jump is set by the vortex strength. However it produces a noticeable change in the slope of the phase variation about the vortex axis and a slight enlargement of the central zone as a increases. The influence of the core size is more pronounced on the amplitude profile where both the width of the central region and the magnitude of the focusing/defocusing effect increase by about 30% when the core size is doubled. Overall the method allows an estimation of the vortex core size with a 10% error, a noteworthy precision considering the high degree of turbulence of the flow.

3.4 Vortex strength

One parameter of the vortex which can be easily varied experimentally is the vortex strength. For a constant rotation rate, one can change the axial pumping in the flow by varying the diameter of the holes that cover the driving discs (see Fig. 1). Figure 9 shows phase profiles for two values of the hole diameter, $2r = 2$ cm and $2r = 5$ cm. We observe that the phase jump increases with r. This implies an increase of the strength of the vortex. Note that as the vortex core size does not change appreciably, it is actually the angular speed about the vortex axis which increases

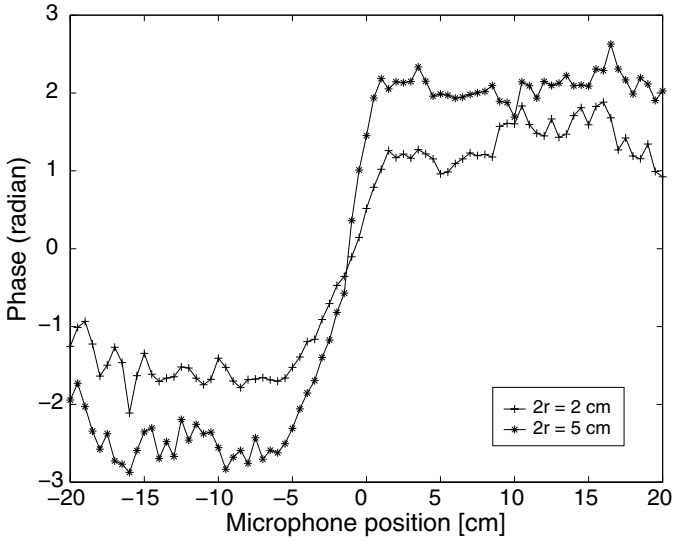

Fig. 9. Influence of the diameter of the disc's holes on the phase signal ($\Omega = 30$ Hz, $\nu_0 = 40$ kHz, $L_2 = 33$ cm).

with the size of the pumping hole in the driving discs. For reasons of stability of the vortex, the diameter $2r = 5$ cm is used in the rest of our measurements.

In fact, the most convenient way to change the strength of the vortex is to operate with a constant geometry and to vary the rotation rate Ω of the driving discs. We have verified that the magnitude of the phase jump, hence the vortex strength is also proportional to Ω.

3.5 Influence of the sound wavelength

We have varied the frequency of the incoming sound wave in the range $\nu_0 \in [40, 80]$ kHz, corresponding to wavelengths varying between 4 mm and 8 mm. Compared with the vortex core size ($a \simeq 30$ mm), the 4 mm wavelength is well within the geometrical approximation, and the 8 mm wavelength is an upper limit, as we will discuss in more details in the next section.

We show in Figure 10a the phase profiles when ν_0 is varied and in Figure 10b the evolution of the corresponding acoustic amplitudes. The overall magnitude of the phase jump as a function of the sound frequency is plotted in the inset. As expected from equation 1, the phase jump varies linearly with increasing sound frequencies. The slope of 7.7×10^{-2} rad kHz^{-1} yields an estimate of the vortex strength $\gamma \simeq 1.4$ m^2 s^{-1}, in very good agreement with the numerical ray-tracing estimation. Although the measurements at low frequency certainly cannot be described by a geometrical acoustics approach, they are included in the inset of Figure 10a because the evolution of the phase jump is aligned on the same straight line as observed at high frequencies.

Regarding the impact of the wave frequency on the amplitude signal, the observations are more complex. In fact, we observe (see Fig. 10b, inset) that the weight of the focusing and defocusing effects depends weakly, if at all, on the wave frequency. In addition, the width of the central

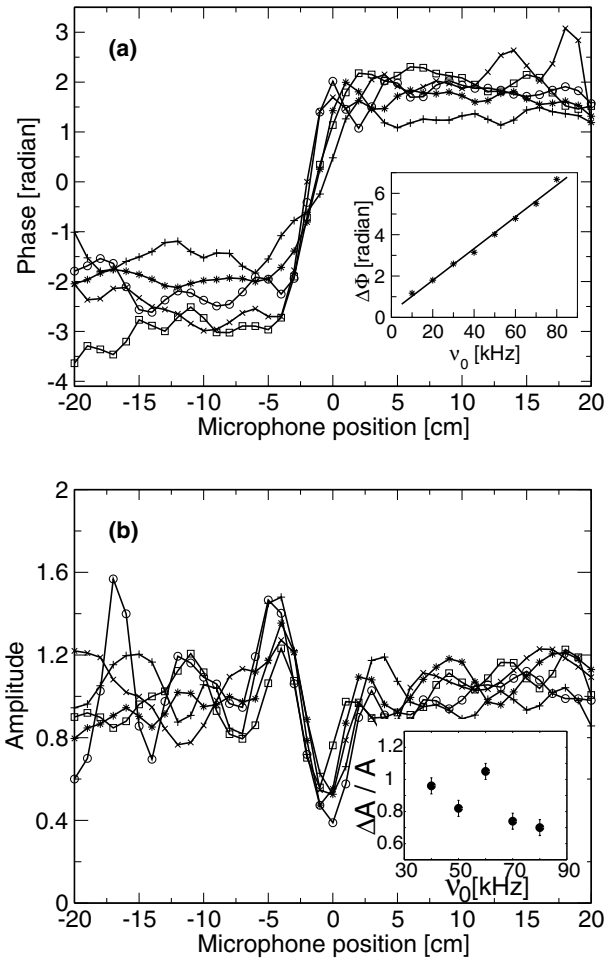

Fig. 10. Influence of the sound frequency on the phase (a) and amplitude (b) profiles. ($\Omega = 30$ Hz, $L_2 = 33$ cm). The inset in (a) shows the variation of the total phase jump with the sound frequency; the straight line is a best linear fit with slope $p \simeq 7.7 \times 10^{-2}$ rad kHz^{-1}. Sound frequencies are 40 kHz (plus), 50 kHz (stars), 60 kHz (circles), 70 kHz (crosses) and 80 kHz (squares).

zone for both phase and amplitude signals are almost constant when the wavelength is varied. These observations are extremely consistent with the geometrical acoustics approximation: the phase varies with the wavelength but not the amplitude which is determined by the ray equation in which the wavelength does not explicitly enter. Note that for the smallest wavelength (about 4 mm), the turbulent fluctuations in the vortex flow could play a role; the fact that they are averaged out in the measurement is an indication that they are incoherent with the large scale dynamics.

3.6 Variation with the downstream distance

We have used the ray-tracing algorithm to compute the sound phase and amplitude profiles in a domain that corresponds to the measurement volume in the experiment. The results are shown in Figures 11 and 12. One can see

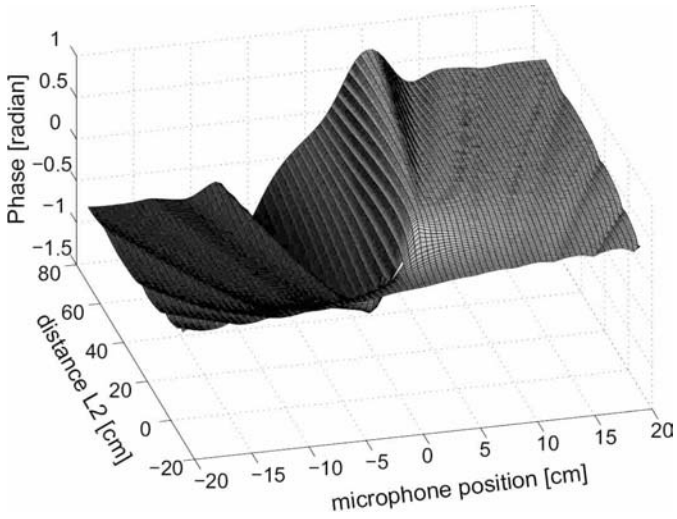

Fig. 11. Phase variation over the whole domain ($\gamma = 1.4\ \mathrm{m^2\,s^{-1}}$, $a = 3$ cm, $\nu_0 = 40$ kHz).

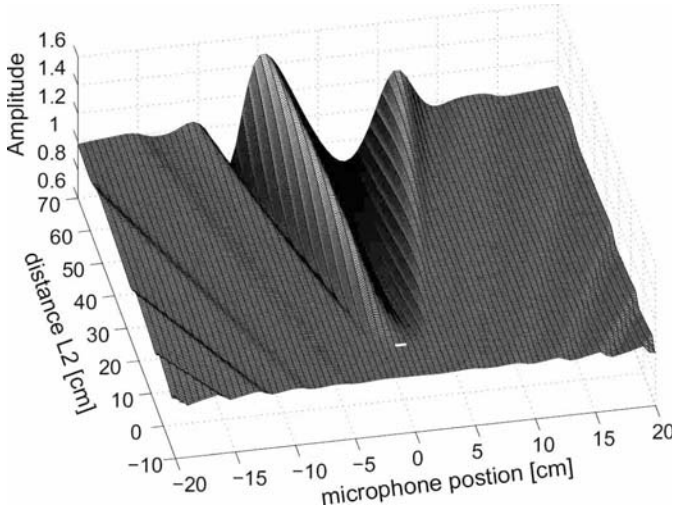

Fig. 12. Amplitude variation over the whole domain ($\gamma = 1.4\ \mathrm{m^2\,s^{-1}}$, $a = 3$ cm, $\nu_0 = 40$ kHz).

that in the geometrical acoustics regime, the phase jump is marked downstream of the vortex as a dislocation in the wavefront (as originally pointed out by M. Berry and co-workers [23]), save for a narrow central region which broadens as L_2 increases. The phase jump thus should not depend on the distance from the vortex axis where the measurement is made. On the other hand, the width of the amplitude fluctuations, broadens slowly in the shadow of the vortex.

To test experimentally these predictions, we have investigated the sound field profiles for $L_2 \in [23, 53]$ cm. We observe in Figure 13 that the phase jump is indeed independent of the distance L_2, while there is a slight increase of the focusing-defocusing effect with L_2. For both phase and amplitude signals we note an increase of the central zone width as predicted by the simulations. When measured on the amplitude the width of the central zone is observed to vary as $1/\sqrt{L_2}$.

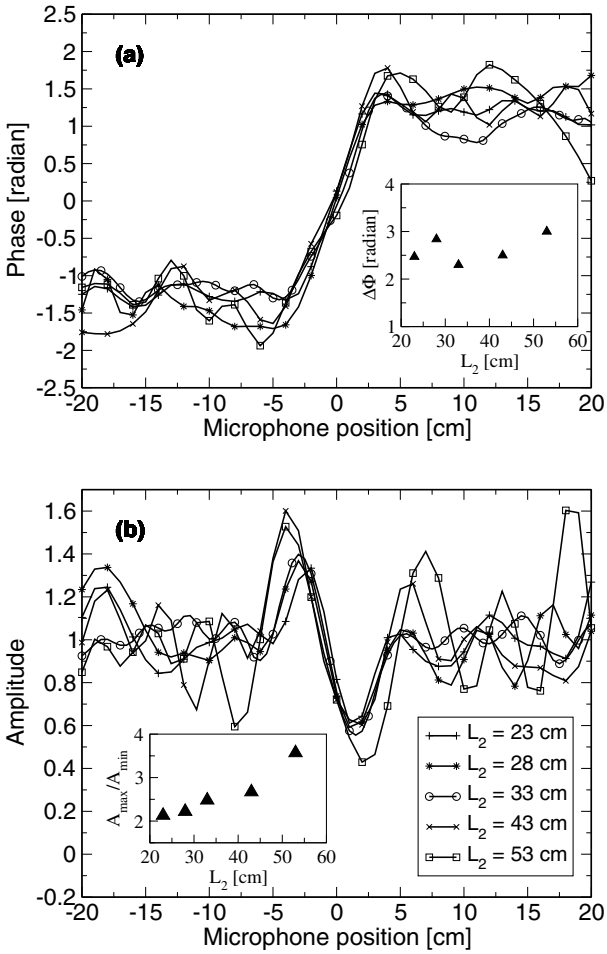

Fig. 13. Phase and amplitude signal over the distance L_2 away from the vortex (experiments), ($\Omega = 30$ Hz, $\nu_0 = 40$ kHz). The inset show the variation of the phase and amplitude jumps with L_2.

4 Scattering effects

In order to investigate effects outside the geometrical acoustics regime, we have repeated the experiments described above, when the frequency of the incoming sound is lowered. We have performed measurements with ν_0 down to 7 kHz, i.e. for wavelengths as large as 5 cm, larger than the vortex core.

We show in Figure 14 the measured amplitude and phase variations downstream of the vortex for an incident sound at 15 kHz. One has $ka \simeq 7$, so that one cannot a priori expect to be in the geometrical acoustics regime. Indeed, one observes clear deviations with respect to the behavior shown in Figure 4 for a small wavelength incident sound. Both the amplitude and the phase have variations of order one over the entire extent of the microphone positions. The order of magnitude of the phase jump is still correctly given by the dimensional argument, but this is mainly due to the fact that the phase is locked to the circulation of the vortex [23]. However, the amplitude has large oscillations, indicating that the angle over which the wavefront is disturbed is very much increased compared

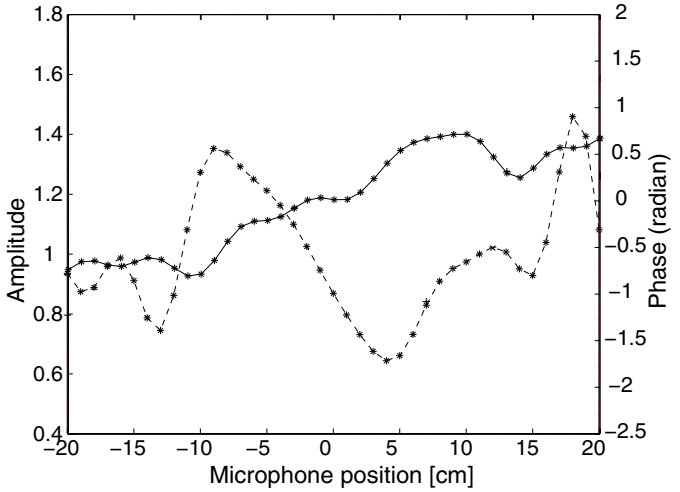

Fig. 14. Amplitude (dashed line) and phase (solid) variations, for an incident sound at a frequency equal to 15 kHz, corresponding to a wavelength $\lambda = 2.3$ cm.

to the geometrical acoustics case. Overall, these effects are a clear indication of diffraction phenomena, i.e. of the scattering of the incident sound by the vortex flow.

The understanding of observations in this regime is much more complex than in the small wavelength limit. Our observations are not made at very large sound wavelengths where Rayleigh scattering theories can be asymptotically derived, but in the intermediate regime where the flow and sound waves have comparable characteristics lengths. In this case, a Born approximation leads to a wave equation such as [6]

$$\left(\partial_t + \boldsymbol{u}_0 \boldsymbol{\nabla}\right)^2 \rho' - c^2 \Delta \rho' = -2\rho_0 \left(\partial_j u_{0,i}\right) \left(\partial_i u'_j\right) \qquad (8)$$

where $\boldsymbol{u}_0$ is the vortex flow and $\boldsymbol{u}'$ the sound perturbation. In the right-hand side term, the acoustic field is often replaced by the incident field. However, it has been emphasized recently [9,11] that in the case of vortices with a non-zero circulation, the long-range azimuthal velocity also advects the incident sound wave and this yields an additional contribution to the scattering field.

In the following we report measurements in which the wavelength and distance to the vortex have been varied and we compare to some analytical and numerical results.

4.1 Evolution with the sound wavelength

In order to study the transition away from the geometrical acoustic regime, we have made measurements at varying incident sound frequencies, $\nu_0 \in [7-50]$ kHz, corresponding to acoustic wavelength ranging from 5 cm down to 7 mm. The results are shown in Figure 15, and for comparison, we display in Figure 16 the corresponding profiles obtained from the ray-tracing simulation.

The agreement between the measured and computed profiles deteriorates as the sound frequency is lowered. The magnitude of the phase jump is correctly given by the dimensional argument ($\Delta\phi = 2\pi\nu_0\gamma/c^2$), but one can

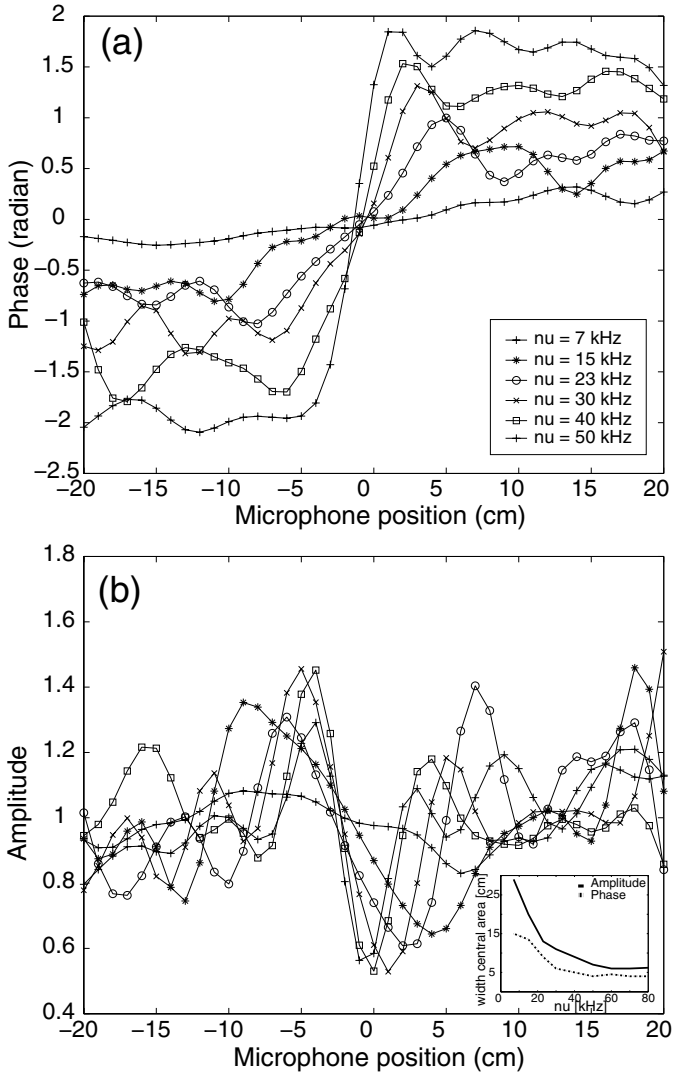

Fig. 15. Phase and amplitude profiles for $\nu_0 \in [7-50]$ kHz. ($\Omega = 30$ Hz, $L_2 = 33$ cm). Experimental measurements.

observe in the measurement of the phase large side oscillations that are not present in the simulation (e.g. profiles at $\nu_0 = 15, 23$ kHz). The value at which the phase saturates broadens as the incident wavelength is increased. The amplitude profiles show even more differences between the experiment and ray-tracing simulations, at low sound frequencies (less than 30 kHz). The experimental amplitude variations are larger, and broader, than what is predicted by geometrical acoustics arguments. In fact, instead of decreasing steadily with ν_0 as in Figure 16b, the amplitude excursion in Figure 15b remains of the order of 50% of the incident sound amplitude. The width of the main scattering lobe, measured as the distance between the local maximum and minimum amplitudes about $x = 0$, decreases sharply with the incident sound wavelength (see inset of Fig. 15). The oscillations in the amplitude have a spatial period that increases with ν_0. The observations of increasing side oscillations and slow amplitude growth with ν_0 are in qualitative agreement with the available analytical far

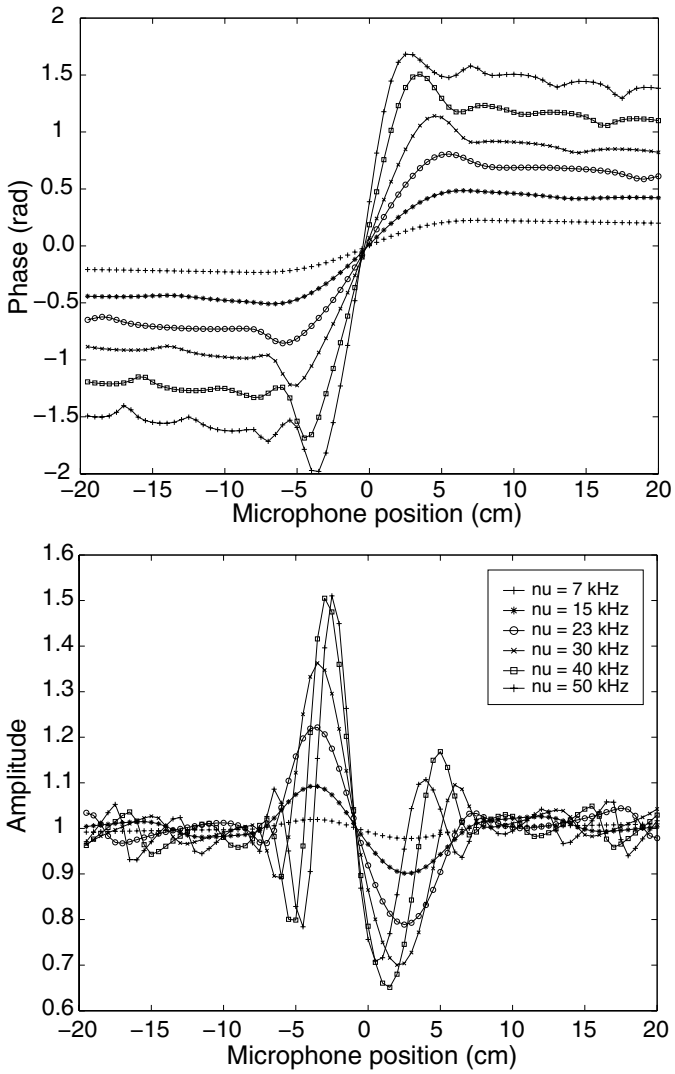

Fig. 16. Phase and amplitude profiles, obtained from ray-tracing simulations, with the same parameters as in Figure 15.

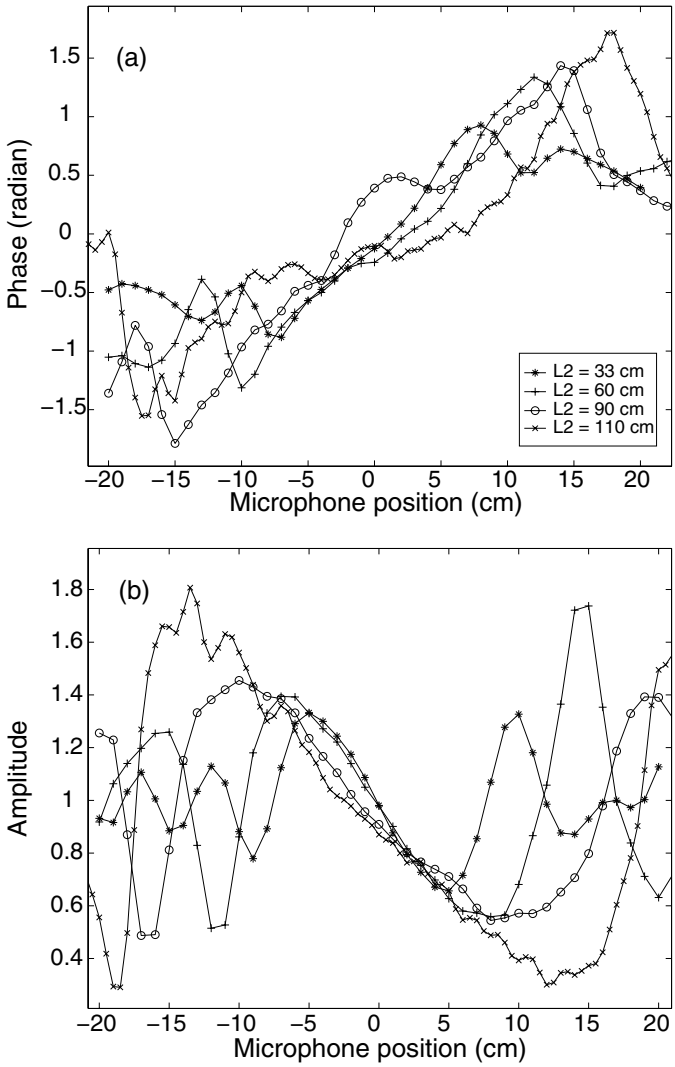

Fig. 17. Variation of the acoustic profiles with the distance of measurement to the vortex core ($\Omega = 30$ Hz, $\nu_0 = 20$ kHz).

field calculations [11] and with the direct numerical simulations [9,10] which take into account the scattering by vorticity.

4.2 Variation with downstream distance

Measurements have been performed at increasing distances downstream of the vortex core, and plotted in Figure 17 (the incoming sound frequency is 20 kHz). In contrast with measurements made at small wavelengths, one observes that the width of the central zone increases with L_2. The variation is linear both for the phase and for the amplitude, and it yields an estimate of the main scattering lobe, $\Delta\theta \simeq 19°$, for the measurement at $\nu_0 = 20$ kHz in Figure 17. This value is in agreement with the numerical results in [9,11] when the sound wavelength is of the order of the vortex core size (at $\nu_0 = 20$ kHz, $\lambda = 1.7$ cm, i.e. about half of the vortex core diameter).

Another feature is that the measured sound amplitude increases with L_2. In Figure 17, the net excursion is about 60% of the incident sound amplitude at $L_2 = 33$ cm, and it reaches 100% at $L_2 = 110$ cm. This is in qualitative agreement with numerical simulations by Berthet [9], but at odds with the study of Ford and Llewellyn-Smith [11] which shows that the scattering cross-section saturates in amplitude as soon as the distance to the vortex exceeds about 10 wavelengths. This matter certainly deserves further investigations. In particular it would be desirable to form vortices with a much smaller core size in order to be able to explore the regime $\lambda \gg a$.

5 Concluding remarks

We have studied the propagation of a monochromatic sound wave through an isolated vortex, in a setup that allows to vary the ratio of the incident sound wavelength to vortex characteristic size. For small wavelengths, our

results are in good agreement with the modeling of propagation using geometrical acoustics approximations. For instance the phase shift on either lateral sides of the vortex is independent of the distance of measurement from the vortex; the amplitude excursion is independent of the sound wavelength. At larger wavelength, scattering effects are clearly identified. Measurement of some features such as the width of the scattering angular lobe are in agreement with recent numerical and analytical work. However a complete study of the scattering regime would require measurements at larger wavelength. Experimentally it is not practical to reduce further the frequency of the incident sound (below 7 kHz ordinary laboratory noise becomes a concern). A solution would be to be able to engineer vortices with a much smaller core size; in air that would result in length scales that would be inside the inertial range of turbulence, as the vortex cannot be laminar if its strength is to remain significant. Such small vortices imbedded in turbulent flows are not stable, making their study much more difficult.

References

1. P.M. Morse, K.U. Ingard, *Theoretical acoustics* (Princeton U. Press, NJ, 1968)
2. D. Blockintzev, J. Acoust. Soc. Am. **18**, 322 (1945)
3. R.B. Lindsay, J. Acoust. Soc. Am. **20**, 89 (1948)
4. L.D. Laudau, E.M. Lifschitz, *Fluid Mechanics* (Pergamon Press, 1959)
5. M.J. Lighthill, Proc. Roy. Soc. London **211**, 564 (1952)
6. See for example, *Sound-Flow interactions*, Lecture Notes in Physics LNP 586, edited by Y. Aurgan, A. Maurel, V. Pagneux, J.-F. Pinton (Springer, 2002)
7. T.M. Georges, J. Acoust. Soc. Am. **51**, 206 (1972)
8. S. Manneville, A. Maurel, P. Roux, M. Fink, Eur. Phys. J. B **9**, 545 (1999); S. Manneville, C. Prada, M. Tanter, M. Fink, J.-F. Pinton, J. Comp. Acoust. **9**, 841 (2001)
9. R. Berthet, *Interaction son-écoulement*, Ph.D. thesis, École Normale Supérieure de Lyon (2001)
10. T. Colonius, S.K. Lele, P. Moin, J. Fluid Mech. **260**, 271 (1994)
11. R. Ford, S.G. Llewellyn Smith, J. Fluid Mech. **386**, 305 (1999)
12. P.R. Gromov, A.B. Ezerskii, A.L. Fabrikant, Sov. Phys. Acoust. **28**, 552 (1982)
13. C. Baudet, S. Ciliberto, J.-F. Pinton, Phys. Rev. Lett. **67**, 193 (1991)
14. M.S. Korman, R.T. Beyer, J. Acoust. Soc. Am. **67**, 1980 (1980)
15. M. Kallistratova, Acoust. Phys. **40**, 429 (1994)
16. B. Dernoncourt, J.-F. Pinton, S. Fauve, Physica D **117**, 181 (1998)
17. C. Baudet, O. Michel, W.J. Williams, Physica D **128**, 1 (1999)
18. R.H. Engler, D.W. Schmidt, W.J. Wagner, B. Weitermeier, J. Acoust. Soc. Am. **71**, 42 (1982)
19. P. Roux, J. de Rosny, M. Tanter, M. Fink, Phys. Rev. Lett. **79**, 3170 (1997)
20. R. Labbé, *Étude de l'écoulement co-rotatif de von Kármán*, Ph.D. thesis, École Normale Supérieure de Lyon (1996)
21. R. Labbé, J.-F. Pinton, Phys. Rev. Lett. **81**, 1413 (1999)
22. M. Oljaca, X. Gu, A. Glezer, M. Baffico, F. Lund, Phys. Fluids **10**, 886 (1998)
23. M. Berry, R.G. Chambers, M.D. Large, C. Upstill, J.C. Walmsley, Eur. J. Phys. **1**, 154 (1980)
24. F. Vivanco, F. Melo, Phys. Rev. Lett. **85**, 2116 (1998)
25. C. Coste, F. Lund, M. Umeki, Phys. Rev. E **60**, 4908, (1999); C. Coste, F. Lund, Phys. Rev. E **60**, 4917 (1999)
26. P.J. Zandbergen, D. Dijkstra, Ann. Rev. Fluid Mech. **19**, 465 (1987)
27. R. Labbé, J.-F. Pinton, S. Fauve, Phys. Fluids **8**, 914 (1996)
28. D. Anke, Acustica **30**, 30 (1974)
29. F. Chillà, J.-F. Pinton, R. Labbé, Europhys. Lett. **34**, 271 (1996)
30. R. Wunenburger, B. Andreotti, P. Petitjeans, Exp. Fluids **27**, 181 (1999)